Characterization of periodic extreme ultraviolet multilayer based on multi-objective evolutionary algorithm

Shang-qi Kuang, Xue-peng Gong, and Hai-gui Yang

Citation: Journal of Applied Physics **122**, 185302 (2017); doi: 10.1063/1.4995806
View online: https://doi.org/10.1063/1.4995806
View Table of Contents: http://aip.scitation.org/toc/jap/122/18
Published by the American Institute of Physics

Characterization of periodic extreme ultraviolet multilayer based on multi-objective evolutionary algorithm

Shang-qi Kuang,[1,a)] Xue-peng Gong,[2] and Hai-gui Yang[3]
[1]*School of Science, Changchun University of Science and Technology, Changchun 130022, China*
[2]*State Key Laboratory of Applied Optics, Changchun Institute of Optics, Fine Mechanics and Physics, Chinese Academy of Sciences, Changchun 130033, China*
[3]*Key Laboratory of Optical System Advanced Manufacturing Technology, Changchun Institute of Optics, Fine Mechanics and Physics, Chinese Academy of Sciences, Changchun 130033, China*

(Received 13 July 2017; accepted 24 October 2017; published online 8 November 2017)

In order to refine the layered structure of extreme ultraviolet multilayers, a multi-objective evolutionary algorithm which is post-hybridized with the standard Levenberg-Marquardt algorithm is applied to analyze the grazing incidence X-ray reflectivity (GIXR) and the normal incidence extreme ultraviolet reflectance (EUVR). In this procedure, the GIXR data and EUVR data are simultaneously fitted as two objectives, and the high sensitivities of these two sets of data to layer thicknesses and densities are combined. This set of mathematical procedures is conducive to obtain a more correct model of periodic multilayers which can simultaneously describe both GIXR and EUVR measurements. As a result, the layered structure of Mo/Si multilayers with a period of about 7.0 nm is obtained. *Published by AIP Publishing*. https://doi.org/10.1063/1.4995806

I. INTRODUCTION

In the last decade, multilayer systems have been investigated as normal-incidence mirrors for soft X-ray and Extreme Ultraviolet (EUV) radiation in the wavelength range from 2 nm to 40 nm. Due to the main application of Mo/Si multilayers in the next generation lithography technology for the semiconductor industry,[1,2] these multilayers have been extensively studied.[1–7] Mo/Si multilayers are usually deposited as periodic stacks of alternating Mo and Si layers, and they also have been used in the fields of astronomy, X-ray microscopy, and X-ray laser.[8,9]

In order to understand and optimize the EUV reflective behavior of Mo/Si multilayers, the characterization of multilayers has already been a subject of intensive research.[3–7] For the periodic multilayer, the traditional characterization usually involves two types of reflective measurements; the first one is grazing incidence X-ray reflectivity (GIXR),[3–7] and the second one is normal incidence extreme ultraviolet reflectance (EUVR).[5,7,10,11] GIXR from the periodic EUV multilayer typically exhibits a series of strong orders that contain a wealth of detailed information about the layered structure, such as the average layer thicknesses, layer densities, and r.m.s. roughnesses. The EUVR measurement is also meaningful because the information of reflectivity at the relevant wavelength is useful for the EUV optical systems. However, both types of measurements have advantages and disadvantages in the structural refinements of multilayers, and the hard X-ray is sensitive to the layer thickness, while it is less sensitive to the chemical composition of the multilayer; the EUV radiation is very sensitive to the chemical components, but the analysis of EUVR data suffers from the multi-solution problem of structural parameters. Therefore, the structural model obtained from the fitting of GIXR data is usually not able to give an accurate prediction of EUVR data, and there are a series of researches which attempted to obtain a consistent model for both GIXR and EUVR data, but these results were not satisfactory.[9,12–15] There are major two reasons for the difficulty in the quantitative analysis of GIXR and EUVR with a single model. The first reason is that the reflectivities at different wavelengths have different sensitivities to the multilayer structural parameters, and the other one is that the solution space defined by the parameterized structure of the multilayer is characterized by many local minima. Recently, an attempt to obtain a single model of the multilayer structure was based on combining the fittings of GIXR and EUVR data, and the Levenberg-Marquardt algorithm was used to optimize the sum of fit goodness of GIXR and EUVR data.[10] It can be understood that an accurate model of the multilayer structure can be obtained when the analyses of GIXR and EUVR data were combined, but we realize that the method that combines these two sets of measurement data is critical. Actually, the curve fittings of GIXR and EUVR are two optimized objectives, and the method to optimize the sum of two fit goodnesses is a classical method which suggests converting the multi-objective optimization problem to a single-objective optimization problem. This approach is direct, but one must give a good consideration of the weight between these two fit goodnesses (or provide optimal numbers of points for both measurements); otherwise, the obtained multilayer structure would tend to give a better simulation for one measurement than the other. Furthermore, the optimized method based on the Levenberg-Marquardt algorithm strongly depends on the initial estimates to find the globally optimum solution, and thus, it should not be advisable to use the best fit model from GIXR analysis as the initial model for the combined fitting.

[a)]Author to whom correspondence should be addressed: physicskuang@sina.com

During recent years, a non-dominated sorting-based multi-objective evolutionary algorithm, called non-dominated sorting genetic algorithm II (NSGA-II), has been developed.[16,17] This algorithm can simultaneously optimize two objectives, and due to the advantage of the evolutionary algorithm, it is immune to local topology in the solution space. Many simulation results on the difficult test problem demonstrate that NSGA-II is able to find a good convergence near the true Pareto-optimal front which is a set of optimal solutions of the multi-objective problem.

In this paper, we demonstrate a procedure for the quantitative structural refinement of a periodic Mo/Si multilayer, and the fittings of GIXR and EUVR data are combined as two objectives of NSGA-II. Due to the advantage of this multi-objective algorithm, one can simultaneously analyze the GIXR and EUVR data without considering the weight between these two fit goodnesses. After the optimization of NSGA-II, a set of optimal solutions of the multilayer structure have been obtained, and these solutions are further used as the initial models for the combined fitting method which is based on the standard Levenberg-Marquardt algorithm.[18] As a result, an optimum solution which is a more satisfactory structure of the periodic Mo/Si multilayer can be obtained. More recently, it is reported that a combination of more complementary measurements has been performed to refine the layered structure of a more complex EUV multilayer,[11] and our approach can also be used to combine other measurements and to characterize other more exotic EUV multilayers. Therefore, our researches should open the applications of the multi-objective evolutionary algorithm on the characterization of multilayers.

II. CALCULATION OF REFLECTIVITY FROM THE PERIODIC MULTILAYER SYSTEM

In this section, a brief description of the electromagnetic wave propagation in a periodic multilayer is given, and here, we focus on the calculation of reflectivity. The wave propagation in a homogeneous layer can be described by the Fresnel equations

$$r_{i,i+1} = \frac{k_i - k_{i+1}}{k_i + k_{i+1}}, \quad \text{s polarization},$$
$$r_{i,i+1} = \frac{k_i/n_i^2 - k_{i+1}/n_{i+1}^2}{k_i/n_i^2 + k_{i+1}/n_{i+1}^2}, \quad \text{p polarization}, \tag{1}$$

where $r_{i,i+1}$ is the Fresnel reflection coefficient between neighboring layers i and $i+1$, and k_i and k_{i+1} represent the z-components of the wave-vectors for layers i and $i+1$, respectively. Here, n_i and n_{i+1} are the complex refractive indexes of the layers i and $i+1$, respectively. In general case, k_i can be written as

$$k_i = \frac{2\pi}{\lambda}\sqrt{n_i^2 - \sin^2\theta}, \tag{2}$$

where λ is the incident beam wavelength and θ is the incident angle. When the propagation of the wave which incidents on a multilayer system is considered, the reflection coefficient r_i of the ith layer which is contained in the multilayer is given by

$$r_i = \frac{r_{i,i+1} + r_{i+1}e^{2i\beta_i}}{1 + r_{i,i+1}r_{i+1}e^{2i\beta_i}}, \tag{3}$$

where $\beta_i = 2\pi d_i\sqrt{n_i^2 - \sin^2\theta}/\lambda$ and d_i is the thickness of the ith layer. If the multilayer system is a series of N layers, the calculation of net reflection coefficient r_0 for the multilayer stack can start from the substrate ($i = N+1$) and use the above recursion formula. Therefore, the reflectivity of the multilayer system can be defined as

$$R = |r_0|^2. \tag{4}$$

Considering the loss in reflectance due to interfacial roughness, the Fresnel reflection coefficient in Eq. (1) should be modified by[19,20]

$$\tilde{r}_{i,i+1} = r_{i,i+1}\exp\left[-\frac{8\pi^2\sigma_{i,i+1}^2}{\lambda^2}\sqrt{(n_i^2 - \sin^2\theta)(n_{i+1}^2 - \sin^2\theta)}\right], \tag{5}$$

where $\sigma_{i,i+1}$ is the interfacial roughness between the layers i and $i+1$. It is worthwhile to point out that formulas in Eqs. (1)–(5) can be used to simulate the GIXR and EUVR curves, and the optical constants were taken from the The Center for X-Ray Optics (CXRO).[21] Specifically, in the simulation analysis of GIXR data, the incidence angle θ should be replaced by the grazing angle $\phi = \pi/2 - \theta$, and the reflected beam intensity is given by

$$I_{\mathrm{GIXR}}^{\mathrm{calc}}(\phi) = R_{\mathrm{GIXR}}^{\mathrm{calc}}(\phi)\cdot I_0 = |r_0|^2\cdot I_0 + I_b, \tag{6}$$

where $R_{\mathrm{GIXR}}^{\mathrm{calc}}(\phi)$ and $I_{\mathrm{GIXR}}^{\mathrm{calc}}(\phi)$ are the calculated reflectivity and reflected intensity of the GIXR measurement, respectively. In Eq. (6), I_0 and I_b are the incident beam and background intensities, respectively.

III. STRUCTURAL MODEL OF THE PERIODIC Mo/Si MULTILAYER AND EXPERIMENT LAYOUT

In the simulations of GIXR and EUVR data, the fitting model of the periodic Mo/Si multilayer consisted of 60 periods with identical parameters and one additional top period with independent parameters to account for the effect of surface oxidation. Hence, the structure of coating can be written as sub/$[Si/MoSi_2/Mo/MoSi_2]_{60}$/Si/$SiO_2$, where the substrate is silicon wafer, and one period is composed of Mo and Si layers and two $MoSi_2$ interlayers.[3–7] Therefore, a set of structural parameters include the periodic thickness d, thicknesses (d_{Si}, d_{Mo}, $d_{\mathrm{Mo\ on\ Si}}$), densities (ρ_{Si}, ρ_{Mo}, $\rho_{\mathrm{MoSi_2}}$), and interfacial roughness σ of the multilayers and the thickness $d_{\mathrm{SiO_2}}$, density $\rho_{\mathrm{SiO_2}}$, and surface roughness $\sigma_{\mathrm{SiO_2}}$ of the top layer. For simplicity, we assume that these two interlayers have the same density as $\rho_{\mathrm{MoSi_2}}$, and the thickness of the other interlayer $d_{\mathrm{Si\ on\ Mo}}$ can be calculated by

$$d_{\mathrm{Si\ on\ Mo}} = d - d_{\mathrm{Si}} - d_{\mathrm{Mo}} - d_{\mathrm{Mo\ on\ Si}}, \tag{7}$$

and then, the thickness of this interlayer is not independent. It is worthwhile to point out that this structural model had been previously used successfully,[3,4] and here, we use this model because it is simple to make the demonstration.

In the experiments, both Mo and Si were deposited using DC magnetron sputtering, and the layer thicknesses were controlled by time which is calculated by pre-calibrated deposition rates. The measured GIXR data of the periodic Mo/Si multilayer were performed on a laboratory diffractometer (PANalytical-Xpert) using CuK_α with the wavelength of $\lambda = 0.15406$ nm. Considering the beam divergence and fluctuation of the direct beam, the systematic error of the GIXR measurement should not exceed 3% of the reflected intensity. The measurement of EUVR was carried out at PTB (Physikalisch Technische Bundesanstalt),[22,23] and the incident angle of the beam was fixed at 1.5°. Considering the accuracy of the EUVR measurement, the total systematic error should not exceed 0.001.

IV. RECONSTRUCTION OF STRUCTURAL PARAMETERS OF THE PERIODIC EUV MULTILAYER

We developed a program based on NSGA-II[16] for the quantitative analyses of GIXR and EUVR data simultaneously, and these two fitness functions are given by

$$\chi^2_{\mathrm{EUVR}} = \frac{1}{N_{\mathrm{EUVR}} - N'} \sum_{\lambda} \frac{\left(R^{\mathrm{mea}}_{\mathrm{EUVR}}(\lambda) - R^{\mathrm{calc}}_{\mathrm{EUVR}}(\lambda)\right)^2}{\sigma^2_{\mathrm{EUVR}}(\lambda)};$$
$$\chi^2_{\mathrm{GIXR}} = \frac{1}{N_{\mathrm{GIXR}} - N'} \sum_{\phi} \frac{\left(R^{\mathrm{mea}}_{\mathrm{GIXR}}(\phi) - R^{\mathrm{calc}}_{\mathrm{GIXR}}(\phi)\right)^2}{\sigma^2_{\mathrm{GIXR}}(\phi)}, \quad (8)$$

where N_{EUVR} and N_{GIXR} are the numbers of measured data points and N' is the number of parameters which describes the layered structure. In Eq. (8), $R^{\mathrm{calc}}_{\mathrm{EUVR}}(\lambda)$, $R^{\mathrm{mea}}_{\mathrm{EUVR}}(\lambda)$, and $\sigma_{\mathrm{EUVR}}(\lambda)$ are the calculated reflectivity, measured reflectivity, and uncertainty of EUVR data, respectively, and $R^{\mathrm{mea}}_{\mathrm{GIXR}}(\phi)$ and $\sigma_{\mathrm{GIXR}}(\phi)$ are the measured reflectivity and measured uncertainty of reflectivity in the GIXR measurement. Here, both uncertainties in the measured GIXR and EUVR data include the systematic and statistical errors.

In this multi-objective evolutionary algorithm, each individual's gene is characterized by the structural parameters of the periodic Mo/Si multilayer, and these parameters are shown in Table I. We use a population size of 100 and run NSGA-II until 500 generations. Other parameters of NSGA-II are crossover probability ($P_c = 0.9$), mutation probability ($P_m = 0.1$), and the distribution indexes for crossover and mutation operators ($\eta_c = 2$ and $\eta_m = 2$, respectively).[16,24] In the following, the conceptual steps of NSGA-II which are suitable for the characterization of the periodic EUV multilayer are given in short, and more details can be found in Refs. 16 and 24.

TABLE I. Model parameters of the periodic Mo/Si multilayer.

	GIXR only	GIXR and EUVR	NSGA-II
d_{Si}/nm	3.70 ± 0.02	3.75 ± 0.01	3.72 ± 0.01
d_{Mo}/nm	1.58 ± 0.03	1.61 ± 0.01	1.78 ± 0.02
$d_{\mathrm{Mo\ on\ Si}}$/nm	1.49 ± 0.02	1.34 ± 0.01	1.11 ± 0.02
d/nm	6.975 ± 0.001	6.9781 ± 0.0002	6.9787 ± 0.0005
$d_{\mathrm{SiO_2}}$/nm	3.0 ± 0.7	3.0 ± 0.5	3.0 ± 0.5
ρ_{Si}/g·cm^{-3}	2.6 ± 0.1	2.31 ± 0.02	2.55 ± 0.03
ρ_{Mo}/g·cm^{-3}	9.1 ± 0.1	10.57 ± 0.03	10.14 ± 0.04
$\rho_{\mathrm{MoSi_2}}$/g·cm^{-3}	6.3 ± 0.1	7.83 ± 0.05	7.61 ± 0.07
$\rho_{\mathrm{SiO_2}}$/g·cm^{-3}	2.6 ± 0.5	2.6 ± 0.3	2.0 ± 0.3
σ/nm	0.347 ± 0.005	0.335 ± 0.002	0.361 ± 0.005
$\sigma_{\mathrm{SiO_2}}$/nm	1.5 ± 0.5	1.5 ± 0.5	2.9 ± 0.5

Step 1. Initialization of the internal multi-objective evolutionary algorithm settings. In this step, all the parameters of the algorithm which have been mentioned above are assigned with values.
Step 2. Creation of a random parent population.
Step 3. Evaluation of the parent population, by calculating these two fitness functions in Eq. (8).
Step 4. Each parent solution is assigned a rank equal to its nondomination level, and the nondominated solutions are further sorted by using the crowding comparison procedure.[16]

If both fitness values of solution p are less than those of solution q respectively, it is defined that solution q is dominated by solution p, which means that solution p is superior to solution q; otherwise, the relationship between these two solutions is nondomination. In this step, each solution is compared with every other solution in the population to find if it is dominated, and this process is continued until all the solutions have finished the comparisons. After this process, one can identify the first set of nondominated solutions, which are defined in the first nondominated level or the first nondominated front. In order to find the individuals in the next nondominated front, the solutions of the first front are discounted temporarily and the above procedure is repeated. With this approach, a population can be sorted into different nondomination levels.

According to the solutions in the same nondominated level, we sort them by comparing their crowding distances. At first, these solutions are sorted according to each objective function value in ascending order of magnitude. Second, for each objective function, the boundary solutions are assigned an infinite distance value; other intermediate solutions are assigned a distance value equal to the absolute normalized difference in the function values of two adjacent solutions. Finally, the overall crowding distance value is calculated as the sum of individual distance values corresponding to each objective, and here, each objective function is normalized by the difference between maximum and minimum values of the objective function before calculating the crowding distance.

Step 5. Creation of the offspring population by using binary tournament selection, recombination, and mutation operators. In this step, the simulated binary crossover operator and polynomial mutation[24] are used.
Step 6. A combined population is formed by the parent and offspring population, and this population is sorted into all different nondominated fronts.
Step 7. New population members are chosen. In the combined population, the solutions belonging to the first

nondominated front are of best solutions, and all members of this front are definitely chosen in the new population. If the size of first nondominated front is smaller than the population size, the remaining members of new population are chosen from subsequent nondominated fronts in the order of their ranking. This procedure is continued until no more nondominated fronts can be accommodated. Generally, the count of solutions in the chosen nondominated fronts would be larger than the population size, and we sort the solutions of the last chosen in descending order and choose the best solutions to fill the new population.

Step 8. Evolution is stopped when the generation is reached; otherwise, this program goes back to Step 3.

After the optimization of the multi-objective evolutionary algorithm, the optimized solutions can be obtained in the first nondominated front. In order to further optimize these solutions, we post-hybridize NSGA-II with the standard Levenberg-Marquardt algorithm[18] to reduce the combined fitness of GIXR and EUVR data, and the combined fitness can be given by

$$\chi^2_{\text{combine}} = \frac{1}{N_{\text{EUVR}} + N_{\text{GIXR}} - N'} \times \left[\sum_{\lambda} \frac{\left(R^{\text{mea}}_{\text{EUVR}}(\lambda) - R^{\text{calc}}_{\text{EUVR}}(\lambda)\right)^2}{\sigma^2_{\text{EUVR}}(\lambda)} + \sum_{\phi} \frac{\left(R^{\text{mea}}_{\text{GIXR}}(\phi) - R^{\text{calc}}_{\text{GIXR}}(\phi)\right)^2}{\sigma^2_{\text{GIXR}}(\phi)} \right]. \quad (9)$$

V. RESULTS AND DISCUSSIONS

In the multi-objective evolutionary algorithm mentioned above, the measured EUVR and GIXR are simulated based on the same model, and the solutions in the first nondominated front corresponding to generations are demonstrated in Fig. 1(a). It is shown that both the fitting values in Eq. (8) can be optimized simultaneously, and because there is no correlation between these two fitness functions during the evolution, we do not need to consider the weight between them. An investigation of Fig. 1(a) demonstrates that all individuals are in the first nondominated front after 300 generations, while after 500 generations, the fitness value of the boundary solution with the best fitting of GIXR data (or EUVR data) is very close to the fitness value of the best solution from only GIXR (or EUVR) fitting. Therefore, there is a good convergence of the solutions to the true nondominated front which is defined as Pareto-optimal front.[16] In the first nondominated front as shown in Fig. 1(a), it is also found that the model with the best fitting of GIXR data usually gives the worst fitting of EUVR data, which is coincident

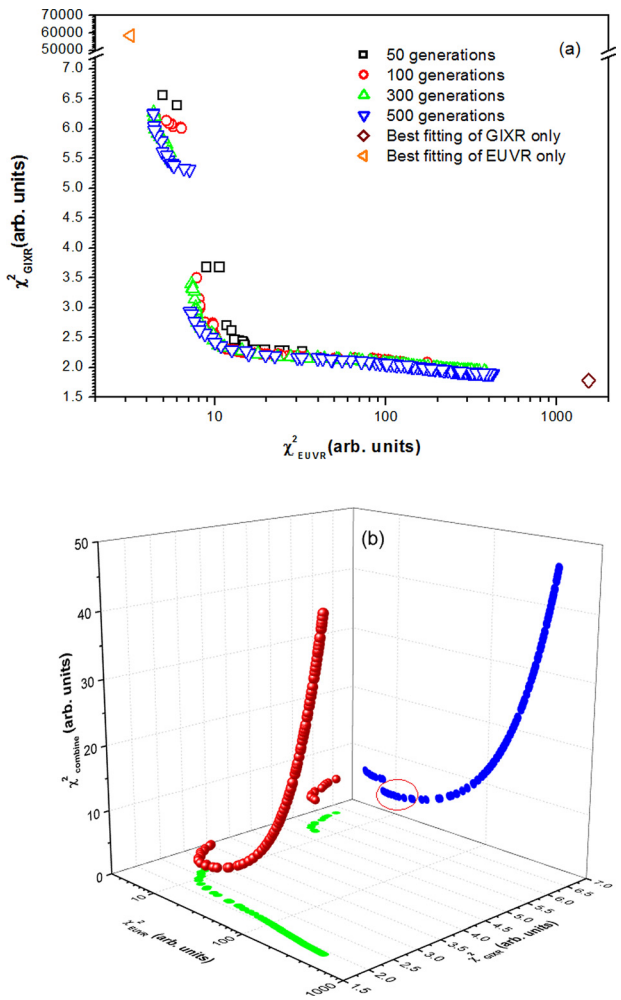

FIG. 1. (a) Obtained nondominated solutions corresponding to different generations of NSGA-II, where the fittings of GIXR and EUVR data are set as two objectives. Here, the best solutions obtained from only GIXR analysis and only EUVR analysis are contained in this graph. (b) Obtained nondominated solutions with NSGA-II after 500 generations (red points), and the vertical axis represents nondominated solution's combined fitness of GIXR and EUVR data. The blue and green points are the backward and horizontal projections of the nondominated solutions, respectively. There is a minimum of combined fitness, and several optimal solutions have close combined fitness. These optimal solutions are selected and emphasized by containing their projections in the backward plane in a red circle.

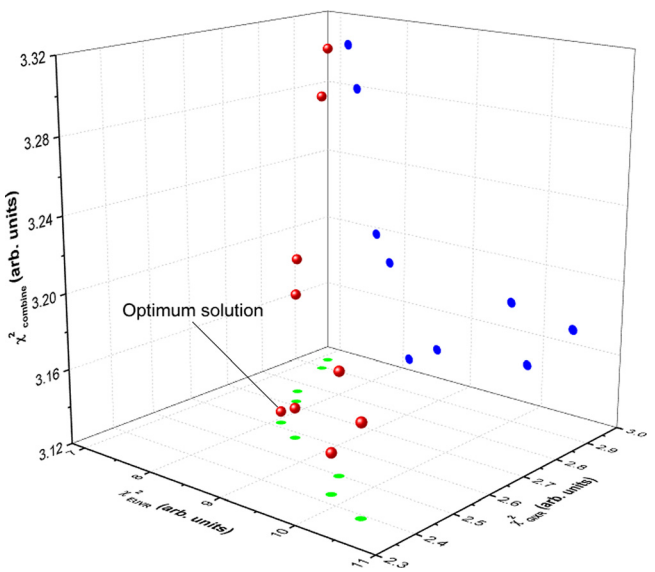

FIG. 2. Obtained solutions with the standard Levenberg-Marquardt algorithm on the optimization of combined fitness of GIXR and EUVR data (red points), and their initial models are selected from the nondominated solutions of NSGA-II as shown in Fig. 1(b). The blue and green points are the backward and horizontal projections of the obtained solutions, respectively, and the solution with the smallest combined fitness is set as the optimum model.

with previous reports.[9,10,12–15] Furthermore, we also found that there is a set of solutions with the close fitness values of GIXR data, but these solutions have very different fitness values of EUVR data. The reason for this result is that the periodic multilayer is a complex system characterized by many structural parameters, and thus, both fittings of GIXR data and EUVR data suffer from the multi-solution problem. Therefore, this combined fitting based on NSGA-II can be useful to supply the reasonable solutions in the nondominated front. In order to distinguish the qualities of solutions in the nondominated front, their combined fitness of GIXR and EUVR data in Eq. (9) are considered, and the results are shown in Fig. 1(b). In Fig. 1(b), the nondominated solutions after 500 generations of NSGA-II are demonstrated as scattered points in the 3D graph, where the horizontal projection of these points is the same graph as shown in Fig. 1(a), and the vertical axis represents the combined fitness. An investigation of Fig. 1(b) demonstrates that the nondominated solutions have different combined fitness functions, which can be found in projections of points in the backward plane.

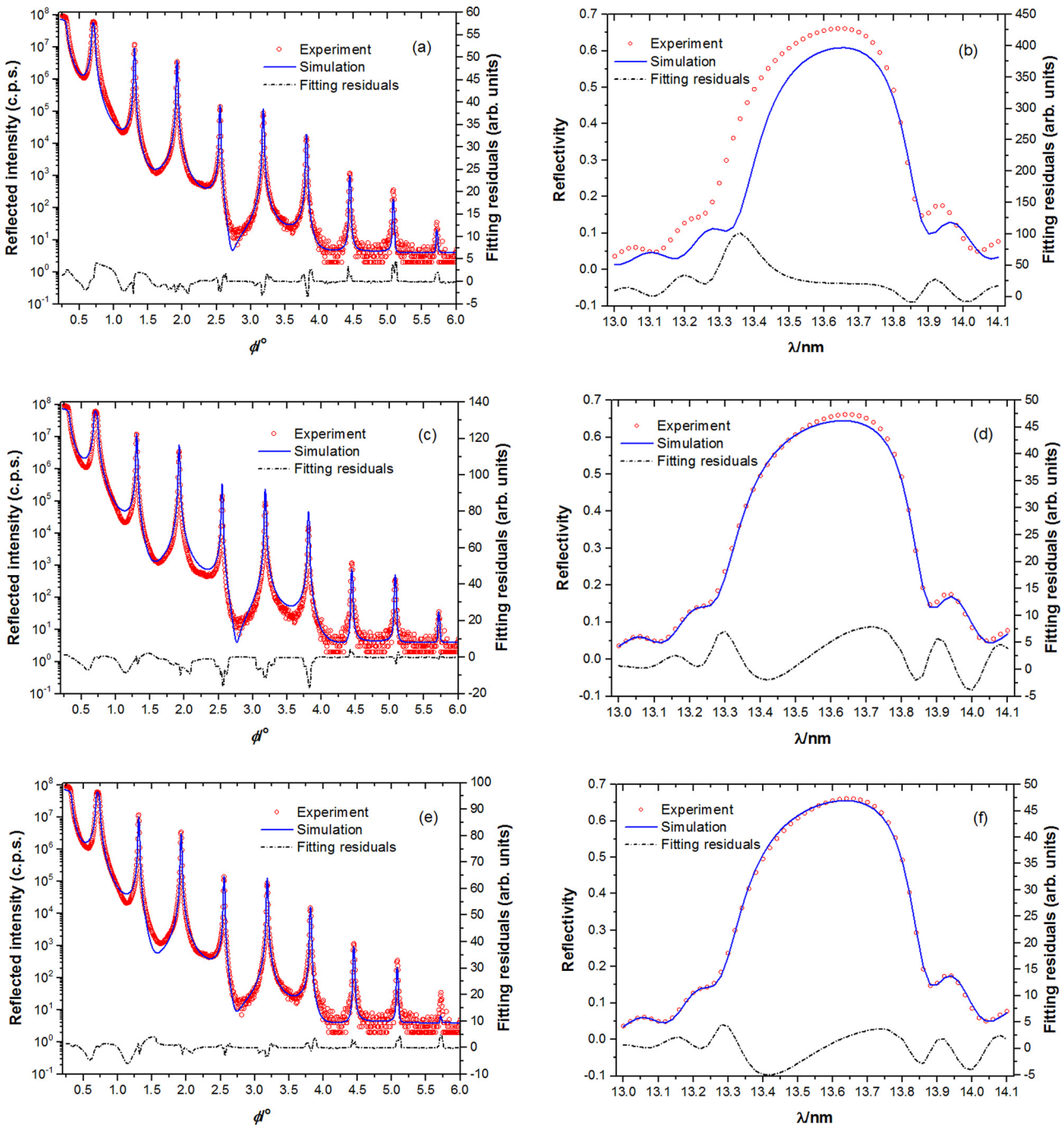

FIG. 3. Experimental profiles, refined calculations, and fitting residuals of the periodic Mo/Si multilayer based on three different structure models. (a) Simulated GIXR curve and fit residuals based on the model from only GIXR analysis. (b) Calculated EUVR curve and fit residuals based on the same model used in Fig. 3(a). (c) Simulated GIXR curve and fit residuals based on the model obtained by the optimization of combined fitness of GIXR and EUVR data, where the best fitting model from only GIXR analysis is used as initial estimates. (d) Calculated EUVR curve and fit residuals based on the same model used in Fig. 3(c). (e) Simulated GIXR curve and fit residuals based on the optimum solution as shown in Fig. 2. (f) Calculated EUVR curve and fit residuals based on the same model used in Fig. 3(e).

Furthermore, there is a minimum of the combined fitness as shown in Fig. 1(b), and several optimal solutions whose backward projections are contained in a red circle have the close combined fitness to the minimum. Therefore, we use these optimal solutions as the initial models for the standard Levenberg-Marquardt algorithm[18] to further reduce their combined fitness. These solutions obtained by the optimization of the Levenberg-Marquardt algorithm are shown as scattered points in the 3D graph of Fig. 2, and here, the solution with the smallest combined fitness is believed to be the optimum solution.

As a contract, the calculated curves of GIXR and EUVR based on the structure models obtained by different methods are presented in Fig. 3. At first, the simulation of GIXR with the best fitting model from only GIXR analysis is demonstrated in Fig. 3(a), and the corresponding parameters are given in Table I. In Fig. 3(a), there is a perfect agreement between the experimental data and fit calculations, but the calculated EUVR curves with the same parameters cannot fit the measurements as shown in Fig. 3(b). This phenomenon has already been found in Fig. 1, and the reasons have also been mentioned above. Second, the simulations of GIXR and EUVR based on the model obtained by the Levenberg-Marquardt algorithm with the initial estimates from only GIXR analysis are demonstrated in Figs. 3(c) and 3(d), respectively, and the corresponding parameters are also given in Table I. Using this model, the fitting of EUVR data becomes much better, but the fitting of GIXR data becomes much worse. However, because the combined fitness becomes smaller, this model is more reliable than the model obtained by only GIXR analysis. Finally, the calculated curves of GIXR and EUVR based on the model which is the optimum solution in Fig. 2 are presented in Figs. 3(e) and 3(f), respectively. It is found that the fittings of GIXR and EUVR data in Figs. 3(e) and 3(f) are better than the fittings in Figs. 3(c) and 3(d), respectively. Therefore, it is believed that the model obtained by our approach should be more reliable and accurate than the above mentioned models. The reason for this result is that the standard minimization algorithm such as Levenberg-Marquardt algorithm tends to get trapped in local minima, and the achievement of the globally optimum solution strongly depends on the initial estimate of the model. Therefore, it should not be advisable to use the best fitting model from only GIXR analysis as the initial model, and the preliminary search for a set of Pareto-optimal solutions becomes a very reasonable step. As a result, this set of mathematical procedures based on NSGA-II should be more reliable to find the optimum model for the simultaneous simulations of GIXR and EUVR data, and the corresponding parameters are also demonstrated in Table I. Comparing the structural models as shown in Table I, it is also found that simultaneous analysis of EUVR and GIXR data significantly increases the accuracy of the determination of the densities of the layers in the multilayer structure. In Table I, the largest increase is observed for the density of the Mo layer, and the reason is the sensitivity of EUVR data to optical contrast between spacer and reflector layers in the multilayer. The increase in the Mo layer density could induce an increase in the EUV reflectivity and a decrease in χ^2_{EUVR}, which are shown in Figs. 3(d) and 3(f). In addition, the thicknesses of interlayers ($d_{Mo\ on\ Si} = 1.11$ nm and $d_{Si\ on\ Mo} = 0.37$ nm) obtained by NSGA-II are consistent with a previous report,[4] and other parameters except the density of the Si layer are more reasonable than the parameters of other models. It is found that the density of the Si layer obtained by NSGA-II is a little higher than bulk density, and the reason is the limitation of our structural model. In our assumption, the interlayers have the same composition of $MoSi_2$, but it was reported that the compositions of the Mo-on-Si and Si-on-Mo interfaces are different.[7] Considering the different compositions of two interlayers, one more parameter of density is needed to describe the extended fitting model. However, because of the strong global searching ability of NSGA-II, the extension of the structural model would not affect the fitting procedure.

VI. CONCLUSION

In summary, a general procedure for quantitative structural refinement of the periodic EUV multilayer based on the multi-objective evolutionary algorithm is presented, and the microstructure of the Mo/Si multilayer with a period of about 7.0 nm is obtained in a more correct model. This research demonstrates a great potential of applications of the multi-objective evolutionary algorithm on the characterization of optical thin films.

ACKNOWLEDGMENTS

This project was supported by the National Natural Science Foundation of China (No. 61405189) and Jilin Scientific and Technological Development Plan (Nos. 20150101019JC and 20170312024ZG).

[1]C. Montcalm, R. Grabner, R. Hudyma, M. Schmidt, E. Spiller, C. Walton, M. Wedowski, and J. Folta, "Atomic-precision multilayer coating of the first set of optics for an extreme-ultraviolet lithography prototype system," Appl. Opt. **41**, 3262–3269 (2002).
[2]E. Louis, A. E. Yakshin, T. Tsarfati, and F. Bijkerk, "Nanometer interface and materials control for multilayer EUV-optical applications," Prog. Surf. Sci. **86**, 255–294 (2011).
[3]A. E. Yakshin, E. Louis, P. Görts, E. Maas, and F. Bijkerk, "Determination of the layered structure in Mo/Si multilayers by grazing incidence X-ray reflectometry," Physica B **283**, 143–148 (2000).
[4]S. Bajt, D. Stearns, and P. Kearney, "Investigation of the amorphous-to-crystalline transition in Mo/Si multilayers," J. Appl. Phys. **90**, 1017–1025 (2001).
[5]A. Aschentrup, W. Hachmann, T. Westerwalbesloh, Y. Lim, U. Kleineberg, and U. Heinzmann, "Determination of layer-thickness fluctuations in Mo/Si multilayers by cross-sectional HR-TEM and X-ray diffraction," Appl. Phys. A **77**, 607–611 (2003).
[6]R. van de Kruijs, E. Zoethout, A. Yakshin, E. Louis, H. Enkisch, G. Sipos, S. Müllender, and F. Bijkerk, "Nano-size crystallites in Mo/Si multilayer optics," Thin Solid Films **515**, 430–433 (2006).
[7]H. Maury, P. Jonnard, J. André, J. Gautier, F. Bridou, F. Delmotte, and M. Ravet, "Interface characteristics of Mo/Si and B_4C/Mo/Si multilayers using non-destructive X-ray techniques," Surf. Sci. **601**, 2315–2322 (2007).
[8]M. Pelizzo, M. Suman, G. Monaco, P. Nicolosi, and D. Windt, "High performance EUV multilayer structures insensitive to capping layer optical parameters," Opt. Express **16**, 15228–15237 (2008).
[9]S. Braun, R. Dietsch, M. Haidl, T. Holz, H. Mai, S. Müllender, and R. Scholz, "Mo/Si multilayers for EUV applications prepared by Pulsed Laser Deposition (PLD)," Microelectron. Eng. **57–58**, 9–15 (2001).

[10]S. Yakunin, I. A. Makhotkin, K. Nikolaev, R. van de Kruijs, M. Chuev, and F. Bijkerk, "Combined EUV reflectance and X-ray reflectivity data of periodic multilayer structures," Opt. Express **22**, 20076–22086 (2014).
[11]A. Haase, S. Bajt, P. Hönicke, V. Soltwisch, and F. Scholze, "Multiparameter characterization of subnanometre Cr/Sc multilayers based on complementary measurements," J. Appl. Crystallogr. **49**, 2161–2167 (2016).
[12]M. Hu, K. Guen, J. André, P. Jonnard, E. Meltchakov, F. Delmotte, and A. Galtayries, "Structural properties of Al/Mo/SiC multilayers with high reflectivity for extreme ultraviolet light," Opt. Express **18**, 20019–20028 (2010).
[13]Q. Zhong, Z. Zhang, J. Zhu, Z. Wang, P. Jonnard, K. Guen, and T. Huo, "The thermal stability of Al(1% wtSi)/Zr EUV mirrors," Appl. Phys. A **109**, 133–138 (2012).
[14]K. Guen, M. Hu, J. André, P. Jonnard, S. Zhou, H. Li, and C. Meny, "Development and interfacial characterization of Co/Mg periodic multilayers for the EUV range," J. Phys. Chem. C **114**, 6484–6490 (2010).
[15]S. Andreev, M. Barysheva, N. Chkhalo, S. Guesev, A. Pestov, V. Polkonikov, D. Rogachev, N. Salashchenko, Y. A. Vainer, and S. Y. Zuev, "Multilayer X-ray mirrors based on La/B_4C and La/B_9C," Tech. Phys. **55**, 1168–1174 (2010).
[16]K. Deb, "A fast and elitist multiobjective genetic algorithm NSGA-II," IEEE Trans. Evol. Comput. **6**, 182–197 (2002).
[17]See http://www.iitk.ac.in/kangal/soft.htm for Multi-objective NSGA-II code in C, Software Developed at Kanpur Genetic Algorithms Laboratory.
[18]W. Press, S. Teukolsky, W. Vetterling, and B. Flannery, *Numerical Recipes in Fortran 77: The Art of Scientific Computing* (Cambridge University Press, 1997), pp. 675–683.
[19]A. Gibaud and S. Hazra, "X-ray reflectivity and diffuse scattering," Curr. Sci. **78**, 1467–1477 (2000).
[20]E. Fullerton, J. Pearson, C. Sowers, S. Bader, X. Wu, and S. Sinha, "Interfacial roughness of sputtered multilayers: Nb/Si," Phys. Rev. B **48**, 17432–17444 (1993).
[21]B. Henke, E. Gullikson, and J. Davis, "X-ray interaction: Photoabsorption, scattering, transmission, and reflection at E=50-30000 eV, Z=1-92," At. Data Nucl. Data Tables **54**, 181–342 (1993).
[22]F. Scholze, J. Tümmler, and G. Ulm, "High-accuracy radiometry in the EUV range at the PTB soft x-ray beamline," Metrologia **40**, S224–S228 (2003).
[23]C. Laubis, F. Scholze, C. Buchholz, A. Fischer, S. Hesse, A. Kampe, J. Puls, C. Stadelhoff, and G. Ulm, "High accuracy EUV reflectometry at large optical components and oblique incidence," Proc. SPIE **7271**, 72713Y (2009).
[24]K. Deb and R. Agrawal, "Simulated binary crossover for continuous search space," Complex Syst. **9**, 115–148 (1995).